International Journal of Multiphase Flow 108 (2018) 80–92

Contents lists available at ScienceDirect

International Journal of Multiphase Flow

journal homepage: www.elsevier.com/locate/ijmulflow

Effect of flow geometry on the evolution of concentrated suspensions flowing through a fracture

Ricardo Medina[a], Russell L. Detwiler[a,*], Romain Prioul[b], Wenyue Xu[b], Jean E. Elkhoury[b]

[a] Department of Civil and Environmental Engineering, University of California Irvine, Irvine, CA, United States
[b] Schlumberger-Doll Research Center, Cambridge, MA, United States

ARTICLE INFO

Article history:
Received 6 January 2018
Revised 3 June 2018
Accepted 18 June 2018
Available online 30 June 2018

MSC:
00-01
99-00

Keywords:
Suspension
Fracture
Polydisperse suspensions

ABSTRACT

Flow of rigid-particle suspensions is prevalent in nature and is important for a range of engineering applications across many disciplines. However, understanding of the three-dimensional flow behavior of suspensions remains limited and studies primarily focus on suspensions consisting of idealized fluids (Newtonian) and particles (neutrally buoyant spheres). Here, we explore the effects of flow geometry on the behavior of a concentrated suspension ($\phi = 0.5$) composed of dense, polydisperse particles suspended in a shear-thinning fluid. Fully developed flow in a tube transitioned through a tapered manifold to a high-aspect-ratio rectangular duct (fracture), which allowed direct visualization of the flow and quantification of the velocity and solid concentration fields. Obstructions added to the fracture led to increasingly three-dimensional flow fields and allowed direct observation of the role of in-plane shear and extension and contraction of the suspension. We observed centimeter-scale reduced-ϕ regions adjacent to the lateral no-flow boundaries and only millimeter-scale reduced-ϕ regions along no-flow boundaries caused by the obstructions placed in the middle of the flow field. This resulted in regions of increased velocity near the lateral no-flow boundaries, but negligible perturbations to the velocity away from the millimeter-scale shear zone along the internal no-flow boundaries. Additionally, recorded ∇P within the fracture exhibited a transient response that persisted throughout the experiment and was independent of the flow rate or obstruction configuration. Simulations using a suspension balance model provided additional insights into the source of the low-ϕ regions and the mechanisms controlling the transient ∇P. The simulation results support the hypothesis that the non-uniform ϕ-distribution developed in the inlet tubing expanded laterally as the suspension flowed through the manifold, creating the low-ϕ (high velocity) regions next to the no-flow boundaries. Additional simulations showed that particle rearrangement across the fracture aperture was directly related to the transient ∇P observed in our experiments.

1. Introduction

Suspensions of non-colloidal, rigid or semi-rigid particles are ubiquitous in a wide range of natural and engineered processes. Examples in natural systems range from the flow of red blood cells suspended in plasma (Bayliss, 1965) to rock crystals suspended in molten lava (Mader et al., 2013). Engineered applications include hydraulic fracturing for oil and gas recovery (Pearson, 1994), soil remediation (Wong and Alfaro, 2001; Murdoch, 1995), removal of drill cuttings (Graham and Jones, 1994; Perez et al., 2004), and the transport of commercial slurries in mining operations (Kaushal et al., 2005). Many of these suspensions involve fluids and particles with non-ideal properties such as non-Newtonian base fluids and particles that may be angular, denser than the fluid, and polydisperse.

Despite the complexities of many suspensions of interest, studies of idealized suspensions (neutrally buoyant, monodisperse spheres suspended in Newtonian fluids) have led to significant insights about suspension rheology. For dilute suspensions (solid volume fraction, $\phi \lesssim 0.2$), hydrodynamic effects induced by the suspended particles cause the viscosity of the suspension, η, to increase relative to the viscosity of the suspending fluid, η_f. This ϕ-dependence is well represented by a first-order linear approximation for suspension viscosity, $\eta = \eta_f(1 + \frac{5}{2}\phi)$ (Einstein, 1906). As ϕ increases, the distance between particles decreases and particle-particle interactions influence η. Different models include the ϕ-dependence of η as ϕ increases beyond the dilute range (Krieger and Dougherty, 1959; Frankel and Acrivos, 1970; Chong et al., 1971). One commonly used model is

* Corresponding author.
E-mail addresses: ricarm3@uci.edu (R. Medina), detwiler@uci.edu (R.L. Detwiler).

https://doi.org/10.1016/j.ijmultiphaseflow.2018.06.014
0301-9322/

the Quemada (1977) model, $\eta = \eta_f(1 - \frac{\phi}{\phi_m})^{-2}$, which accurately predicts observations of $\eta(\phi)$ for suspensions with particle concentration in the range $0.15 \lesssim \phi < \phi_m$, where ϕ_m is the maximum solid volume fraction, e.g., the concentration at which the suspended solids jam, or cease to flow with the suspending fluid. As the suspension concentration approaches the jamming limit, $\phi \to \phi_m$, viscosity increases sharply.

In addition to exhibiting strong ϕ dependence, the viscosity of suspensions often exhibits dependence on shear rate, $\dot{\gamma}$. Rheology measurements of neutrally buoyant spheres suspended in Newtonian fluids have demonstrated shear-thinning behavior that is most evident in suspensions with $\phi \gtrsim 0.4$ (Leighton and Acrivos, 1987; Zarraga et al., 2000). Gadala-Maria and Acrivos (1980) observed a transient response of an ideal suspension subjected to a simple shear in the gap between two concentric cylinders and hypothesized that shear gradients caused particles to migrate out of the gap, reducing both ϕ and η. Those results suggested that the $\dot{\gamma}$-dependence of η for suspensions in Newtonian fluids is due to rearrangements in the microstructure of the particles (or local concentration).

These previous studies in ideal suspensions also inform our understanding of non-ideal suspensions. When particles are suspended in a non-Newtonian fluid with $\dot{\gamma}$-dependent viscosity, the suspension viscosity generally exhibits similar $\dot{\gamma}$ dependence, but the magnitude of the viscosity for a given shear rate increases with ϕ (Metzner, 1985; Dagois-Bohy et al., 2015; Pal, 2015). Experimental measurements suggest the viscosity increase with ϕ at zero shear rate ($\dot{\gamma} \to 0$) follows the Quemada (1977) model, such that $\eta(\phi, \dot{\gamma})\big|_{\dot{\gamma}\to 0} = \eta_f(1 - \frac{\phi}{\phi_m})^{-2}$. Polydisperse suspensions exhibit similar flow characteristics to those of monodisperse suspensions. However, smaller particles may fill the voids between larger particles, and thus increase ϕ_m. Experimental observations suggest the viscosity of bi-disperse suspensions of spherical particles only depends on the relative solid volume fraction (ϕ/ϕ_m) and not the particle size distribution (Chong et al., 1971). Stokesian-dynamics simulations verified these results and extended them to multi-modal distributions (Chang and Powell, 1993).

More detailed measurements of suspension rheology in ideal suspensions under simple shear have revealed shear-induced differences in normal stresses, Σ_{ii} (where $i = 1, 2, 3$ are defined for a simple shear as 1-velocity, 2-velocity gradient, and 3-vorticity directions), which result from hydrodynamic interactions or direct contact between particles (Morris and Boulay, 1999; Siginer, 2015). Of particular interest are the first and second normal stress differences, defined as $N_1 = \Sigma_{11} - \Sigma_{22}$ and $N_2 = \Sigma_{22} - \Sigma_{33}$, respectively. These normal stress differences are typically negative, with $|N_2| > |N_1|$ for monodisperse suspensions and both scale with shear stress and ϕ (Morris and Boulay, 1999; Zarraga et al., 2000; Boyer et al., 2011; Garland et al., 2013). However, recent experiments have measured positive values of N_1, which suggests that further experiments are needed to gain a full understanding of shear-induced normal stress differences in suspensions (Dbouk, 2013; Gamonpilas et al., 2016). These shear-induced normal stress differences also cause particles to migrate relative to the bulk motion of the suspension. Such particle migration has been observed in two-dimensional simple shear flows, such as Couette rheometers (Gadala-Maria and Acrivos, 1980; Leighton and Acrivos, 1987) and wide-gap Couette flows (Phillips et al., 1992; Abbott et al., 1991), where the particles migrate from regions of high shear rate to regions of low shear rate.

Modeling suspension flow requires effectively incorporating the dependence of η on both ϕ and $\dot{\gamma}$, and their dependence on shear-induced normal stress differences, resulting in migration of particles within the suspension. Leighton and Acrivos (1987) proposed that shear-induced particle migrations were akin to a diffusive process controlled by an imbalance of particle interactions, which are affected by shear-rate, viscosity, and concentration gradients. This concept was formalized by Phillips et al. (1992) into what is known as the 'diffusive flux model'. Nott and Brady (1994) proposed an alternative 'suspension balance model' (SBM), which couples mass, momentum, and energy conservation of both the solid and suspension phases to explain these shear-induced particle migrations. In this model, the shear-induced particle migrations arise from the requirement of momentum balance in the presence of shear-induced normal stress differences (Nott and Brady, 1994; Brady and Morris, 1997). The original SBM model only accounted for isotropic normal stresses; Morris and Boulay (1999) proposed the introduction of a 'normal viscosity', modifying the SBM to include anisotropic normal stresses. With these modifications, the SBM accurately predicts shear-induced particle migrations in any two-dimensional flow, including truncated cone-and-plate torsional flow (Chow et al., 1995) and parallel-plate torsional flow (Chapman and Leighton, 1991). Experiments involving pressure-driven suspension flow in two-dimensional geometries (tubes and parallel plates) also demonstrate shear-induced migration of particles from regions of high shear rate to regions of low shear rate (Abbott et al., 1991; Koh et al., 1994; Hampton et al., 1997; Lyon and Leal, 1998; Lecampion and Garagash, 2014; Oh et al., 2015). The result is particle migration away from the walls towards the center line and a corresponding flattening of the velocity profile in the center of the flow. Such observations have been accurately predicted by SBM simulations in simple two dimensional flows where there is only one shear component (Miller and Morris, 2006; Dbouk, 2013).

Efforts to quantify behavior of concentrated suspensions in three-dimensional flow fields have largely relied upon computational simulations. Reddy and Singh (2014) and Yadav et al. (2015) studied concentrated suspension flows in a bifurcating square channel, by applying the diffusive flux model to this three-dimensional flow problem. Though this model does not correctly account for curvilinear flows, they argued that the extensional region of the flow occurring at the bifurcation of the channel is short relative to the length of the flow domain and thus insignificant. Their results predict that the concentration distribution in the branched channels is flattened as the bifurcation angle increased, which significantly changed the shear stress distribution at the walls. Medina et al. (2015) conducted flow-through experiments of a concentrated suspension through a high-aspect-ratio (width to height, $W/h \approx 34$) rectangular duct to study proppant transport in fractures. Note, these experiments differed significantly from previous studies involving Poiseuille suspension flow, such as Lyon and Leal (1998), where the aspect ratio was $\mathcal{O}(1)$. They observed the development of high-velocity ($\sim 2\times$ the mean velocity) regions near the fracture edges where one would expect velocity to be the lowest. They hypothesized that these high velocity regions were caused by a reduction in solid volume fraction in these regions, which was caused by the tapered inlet manifold that created a region of extensional flow between the inlet tubing and fracture, however, their experiments were unable to directly measure this region of extensional flow.

Here, we present results from a set of experiments in which we systematically increase the degree of three dimensionality of flow through a high-aspect-ratio fracture. It is reasonable to expect that, locally, the ϕ and velocity distributions will be similar to those observed in tubes and parallel-plate systems where $W/h \approx 1$, but our previous results (Medina et al., 2015) suggest that variations across the fracture width may significantly influence suspension flow. We explore the potential effects of three-dimensional flow geometries on the behavior of concentrated ($\phi = 0.5$), polydisperse, dense particles suspended in a shear-thinning base fluid, similar to suspensions of proppants used during hydraulic fractur-

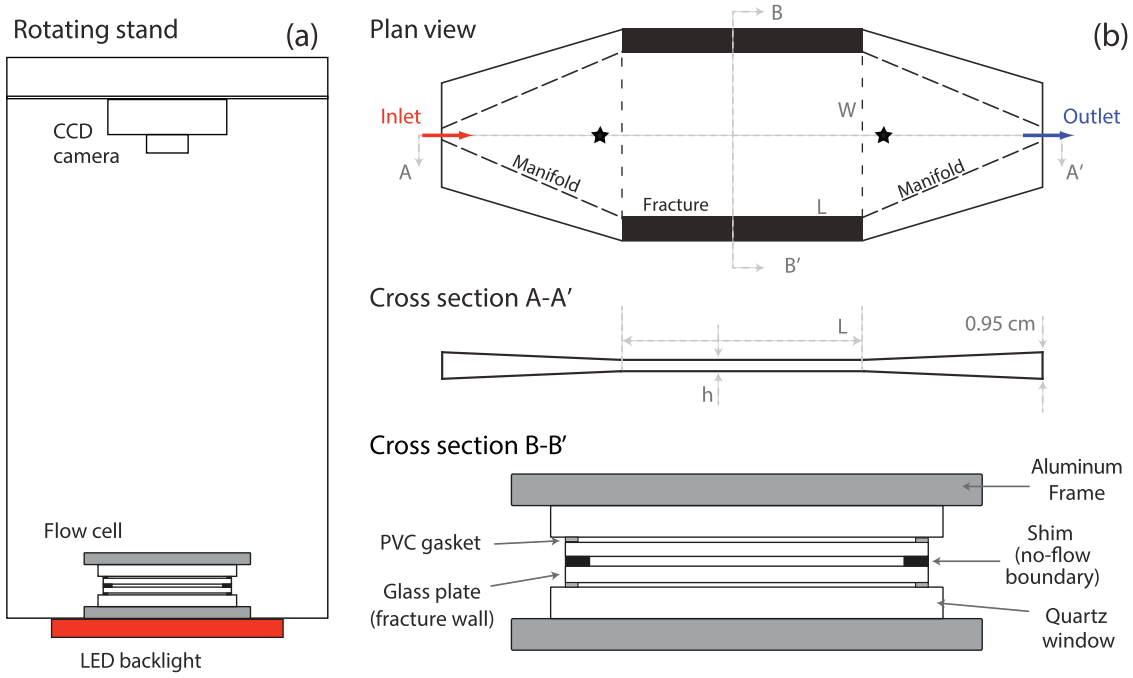

Fig. 1. (a) Schematic of the rotating stand housing the flow cell, LED panel, CCD camera, and controllers (not shown). (b) Schematic of the flow cell showing the transparent parallel-plate fracture and manifold configuration. The manifold gradually tapers from the inlet/outlet tubing to the fracture geometry. The inlet (red arrow) and outlet (blue arrow) are connected to a 0.95 cm i.d. flexible tube. The pressure ports (black ⋆'s) were connected to a differential pressure transducer. (For interpretation of the references to colour in this figure legend, the reader is referred to the web version of this article.)

ing. We added simple obstructions to the flow field to systematically study three-dimensional flows that induce extensional and compressional flow components and shear-rate gradients in multiple directions. The base case is an obstruction-free parallel-plate fracture with inlet and outlet manifolds that induce extension and compression of the flow, respectively. The second experiment includes a thin-plate obstruction, oriented parallel to the flow direction and placed in the center of the fracture, which adds shear-rate gradients in the fracture plane but only causes minor deviation of the largely two-dimensional velocity field. The third experiment includes two symmetric thin-plate obstructions oriented at an angle to the mean direction of the flow, which create significant velocity gradients in the plane of the fracture. In all cases the four walls (e.g., top/bottom fracture surfaces and no-flow boundaries) create shear-rate gradients in both directions normal to the mean flow direction. We use transmitted light techniques to estimate ϕ within the fracture and particle image velocimetry to measure velocity fields during each experiment. To extend our analysis of the experimental results, we also present suspension-balance-model simulations in two different idealized channel geometries.

2. Methods

We explored the flow behavior of concentrated suspensions of dense particles flowing through an analog fracture using an experimental apparatus that allowed quantitative visualization of the entire flow field (Medina et al., 2015). Here, we briefly describe the experimental apparatus, the details of the suspension, the experimental procedure, and image processing techniques.

2.1. Experimental apparatus

We used a rotating stand with a high-resolution charged-coupled-device (CCD) camera (Photometrics Quantix KAF-6303e) mounted directly above a monochromatic red (wavelength, $\lambda =$ 625 nm) LED panel (Fig. 1a). Two fracture surfaces (15.24 cm $\times$ 15.24 cm $\times$ 1.2 cm smooth glass plates) were separated by two aluminum shims (1.91 cm $\times$ 15.24 cm) which acted as no-flow boundaries along the fracture edges and provided a uniform fracture aperture of $\sim$0.3 cm. Two 2.5-cm-thick fused-quartz windows supported by 2.5 cm-thick aluminum frames clamped the fracture surfaces together (Fig. 1b). Steel clamps secured the fracture assembly (flow cell) to the stand between the light source and the camera. An electronic controller synchronized 65-ms pulses of the LED panel with exposure of the CCD camera to provide reproducible images of the fracture. The CCD camera used 12-bit digitization of the measured intensities. Linear pixel size of the recorded images was 76 μm.

We carried out a set of three experiments in the same parallel-plate fracture under the same experimental conditions, the only difference was the obstruction configurations (Fig. 2). The inlet manifold was connected to a 0.95-cm i.d. flexible tube, and tapered gradually from the inlet port (red arrow) to a slot of the same width (W) and aperture (h) as the fracture; a similar manifold was placed on the outlet side of the fracture (Fig. 1b). A differential pressure transducer connected to the ports located at the center of the inlet and outlet manifolds (marked by a ⋆ in Fig. 1b) measured the differential fluid pressure (ΔP) between the inlet and outlet side of the fracture at a sampling interval of 3 s. The distance between the pressure ports was 20 cm. The base case was Experiment A, in which the suspensions flowed through a parallel plate fracture without obstructions inside the fracture (Fig. 2a). Results from Experiment A were previously reported by Medina et al. (2015). Experiment B, included a 10-cm long aluminum obstruction placed in the middle of the fracture, parallel to the mean direction of flow (Fig. 2b). Experiment C included two obstructions in the center of the fracture oriented at an angle of $\pm 27°$, the leading edges of the obstructions were 1.0 cm apart while the trailing edge of the obstruction was 2.0 cm away from the no-flow boundary (Fig. 2c). The leading edges of all obstructions were sharp to reduce the potential for developing a stagnation or jamming zone (Fig. 2d).

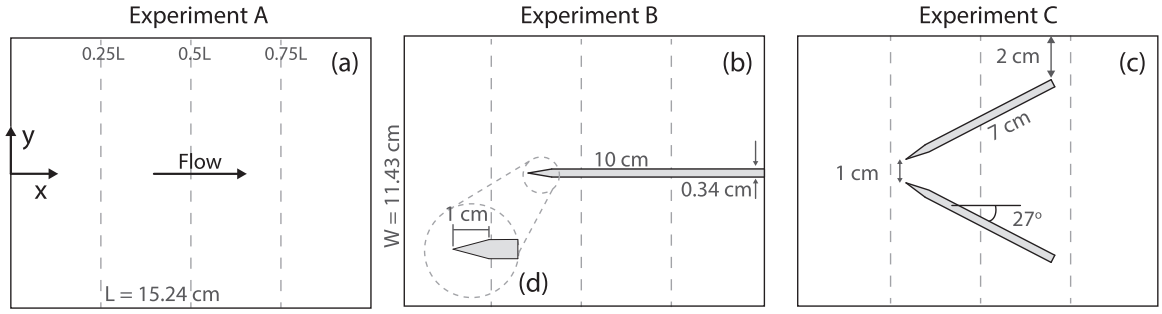

Fig. 2. Plan view schematic showing the location and orientation of obstructions within the fracture for the three different experiments: (a) Experiment A, with no obstructions, (b) Experiment B, single obstruction aligned parallel to the flow direction, and (c) Experiment C, two obstructions at an angle of 27 degrees from the centerline of the fracture. The insert (d) shows the details of the leading edge of the obstructions. In all experiments flow was from left to right. Vertical dashed lines represent the sampling locations used in Fig. 7.

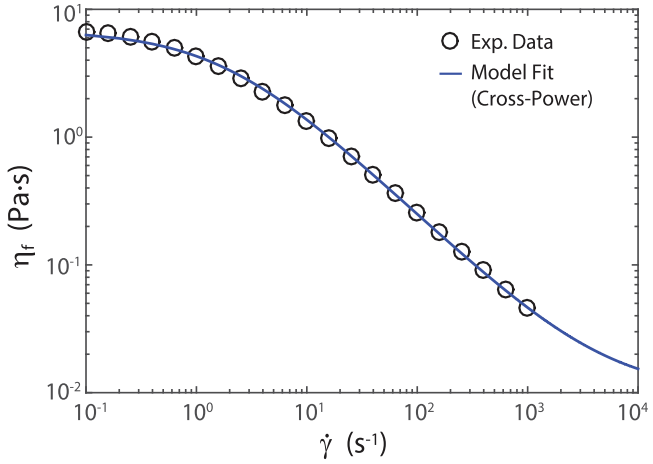

Fig. 3. Experimental and modeled viscosity of the 0.75% guar-water carrier fluid. The experimental viscosity is approximated by the Cross-power law model: m = 0.534 s, n = 0.833, η_{f_o} = 6.844 Pa.s, and η_{f_∞} = 0.01 Pa.s.

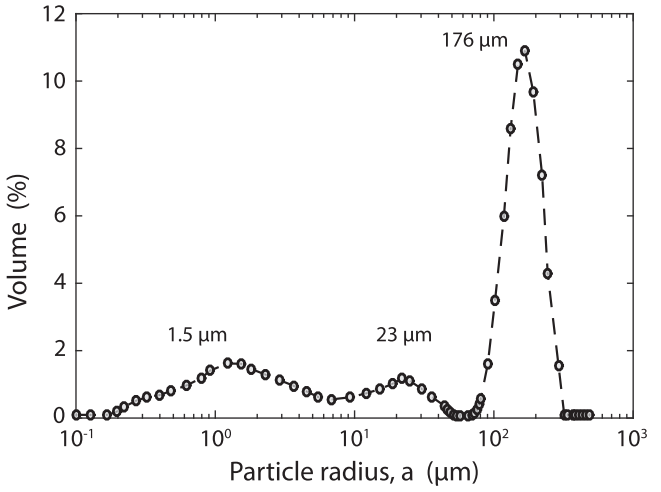

Fig. 4. Multimodal particle size distribution (PSD) used in concentrated suspension experiments. The particle size distribution has three main modes at a = 1.5 µm, a = 23 µm, and a = 176 µm, respectively.

2.2. Concentrated suspension details and preparation

The carrier fluid for the suspension was a guar-gum and water mixture, with a 0.75% (w/w) guar-to-water ratio and a density of ρ_f = 1190 kg/m^3. We prepared the base fluid by mixing guar and water in a laboratory-grade blender (Waring 7012 g). The solution was mixed for at least 10 min to ensure complete hydration of the guar. The carrier fluid was then placed under vacuum for approximately 12 h to remove air bubbles entrapped during mixing. We measured the viscosity of the guar solution at 23°C using a parallel plate rheometer at shear rates in the range $\dot{\gamma} = 0.01 - 1000$ s^{-1}. To assess the stability of the fluid rheology, we repeated this process 7 times with sample ages ranging from 5 to 269 h from completion of the initial mixing process. The measurements are represented well by the Cross-power law model, $\eta_f = \frac{\eta_{f_o} - \eta_{f_\infty}}{1+(m\dot{\gamma})^n} + \eta_{f_\infty}$, where m is the fluid relaxation time, n is the power-law index, η_{f_o} and η_{f_∞} are the viscosity at zero and infinite shear rate, respectively (Chhabra, 2006). Least-squares fitting for the 5-hour measurements yielded parameter values of m = 0.534 s, n = 0.833, η_{f_o} = 6.844 Pa.s, and η_{f_∞} = 0.01 Pa.s (Fig. 3). Fitted values of η_{f_o} exhibit an exponential decay with a time constant of ~200 h indicating an approximately 5% decrease in the fluid viscosity over the duration of each fracture flow-through experiment.

We prepared the concentrated suspension by adding 50% (v/v) silica sand (ρ_p = 2600 kg/m^3) to the de-aired carrier fluid. The sand had a multimodal size distribution with three distinct nominal particle radii of 176 µm, 23 µm, and 1.5 µm (Fig. 4). Such multimodal PSD is representative of the solids used in hydraulic fracturing fluids. A rotary mixing paddle mixed the suspension as we slowly added sand to the carrier fluid. A lid with a vacuum-tight pass-through for the mixing paddle sealed the container, and the paddle mixed the concentrated suspension under vacuum for approximately 15 min to ensure a well-mixed and de-aired suspension. We minimized solids settling by transferring the suspension into a syringe pump and beginning the flow-through experiment immediately after mixing. The syringe pump consisted of a clear polycarbonate pipe (2.5 m long, 2.5 cm inner diameter) fitted with a plunger. A plastic funnel secured to the bottom of the pipe provided a smooth transition from the 2.5-cm inner-diameter pipe to a 0.95-cm inner-diameter tubing. Water pumped into the opposite end of the polycarbonate pipe displaced the plunger and pushed suspension through the funnel and into the fracture at specified volumetric flow rates.

2.3. Procedure for flow through experiments

For each of the flow experiments, we completed the following steps: (1) with the fracture oriented vertically, filled the inlet tubing and fracture with carrier fluid while taking care to avoid introducing air bubbles that could affect flow and induce optical artifacts; (2) acquired reference images of the fracture filled with carrier fluid; (3) connected the tube from the syringe/funnel to the inlet port on the manifold and rotated the stand 90 degrees to orient the fracture horizontally; (4) initiated image and data

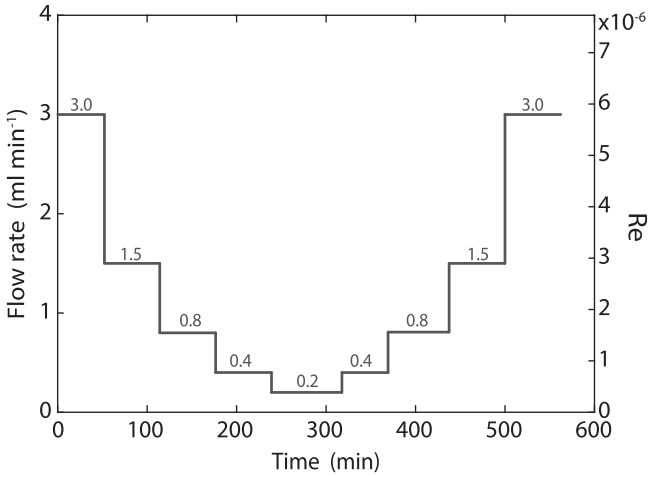

Fig. 5. Schematic showing the sequence and approximate duration of each flow rate step.

acquisition and started flow of the concentrated suspension at a flow rate of 6.0 ml min^{-1}; and (5) increased light intensity after the fracture was uniformly filled with the concentrated suspension to enhance contrast between solids and surrounding carrier fluid. The flow experiment was then conducted by stepping the flow rate through a sequence of decreasing and increasing target flow rates (Fig. 5). Recorded flow rates fall within 3% of the target flow rates. At each step, we changed the flow rate after the flow had reached a quasi-steady state based on the measured ∇P and flow rate, which occurred approximately 50–60 min after the initial flow rate change. While carrying out Experiment A, we experienced a data-acquisition malfunction, which resulted in some erroneous pressure readings. The issue was resolved before carrying out any further experiments. The recorded pressure data in Experiment B had small-amplitude periodic oscillations. Filtering these oscillations in post-processing showed qualitatively similar results to those in Experiment C, which involved only a brief data acquisition lapse. During these data-acquisition lapses, only ∇P measurements were affected; the pump, in-flow/out-flow balances, and image systems continued to function properly.

2.4. Image analysis

Images captured with the CCD camera measured light-intensity values, which we later converted to light absorbance. Using absorbance allows quantitative comparison of images between experiments by eliminating any spatial variations in light-source intensity. Additionally, absorbance can be used to quantify the aperture and ϕ within the flow field. Post-processing of images corrected small registration errors and temporal variations in emitted light intensity (Detwiler et al., 1999).

2.4.1. Aperture measurement

We used light transmission techniques to measure the fracture aperture field. Though the fracture consisted of two smooth glass plates, small long-wavelength variations in the glass are common; using high-resolution images and light transmission techniques allowed us to measure these fracture aperture variations. Light absorbance is related to light intensity by applying the Beer–Lambert law to measurements of the fracture filled with clear and dyed water:

$$A_{i,j} = \ln\left(\frac{I_{c_{i,j}}}{I_{d_{i,j}}}\right) \tag{1}$$

where $A_{i,j}$ is the absorbance in pixel (i, j), I_c and I_d are measured light intensity of the fracture filled with clear and dyed water, respectively. We measured the mean fracture aperture by injecting a known volume of fluid, V_f, into a vertically oriented fracture and measured the total area covered by the injected volume, A_f (for a detailed description see Medina et al., 2015; Medina et al., 2016). We then calculated the mean fracture aperture, $\langle h\rangle = V_f/A_f$, and the spatial distribution of aperture within the fracture (Detwiler et al., 1999):

$$h_{i,j} = \frac{A_{i,j}}{\langle A\rangle}\langle h\rangle \tag{2}$$

where h is the fracture aperture, A is the absorbance, and $\langle\cdot\rangle$ represents spatial averaging. The measured average aperture, $\langle h\rangle$, for all the experiments was $\sim$3450 μm. Measurements also revealed a small (long-wavelength) spatial variation of approximately 50 μm, with smallest apertures near the no-flow boundaries.

2.4.2. Solid volume fraction measurement

We can derive a relationship to quantify ϕ, based on the measured light absorbance using light absorption and scattering theory (Bohren and Huffman, 2008). Treating the flowing suspension inside the fracture as a 'slab' of particles, we can relate the absorbance to the solid concentration by:

$$A = n_s C_{\text{ext}} h \tag{3}$$

where h is the fracture aperture and the absorbance is now defined as $A = \ln(\frac{I_{cf}}{I_s})$, where I_{cf} and I_s are the light intensity through the carrier fluid and suspension, respectively. The particle number density of sand or number of particles per unit volume, n_s, can be approximated by assuming spherical grains, which leads to $n_s = \phi\frac{3}{4\pi a^3}$. C_{ext} is the extinction cross section of the sand particles, which is a measure of total light attenuated by the particles, including attenuation due to scattering and absorption. Using this definition of n_s and rearranging terms, Eq. (3) reduces to:

$$A = \phi\frac{3C_{\text{ext}}}{4\pi a^3}h = \phi\alpha_s h \tag{4}$$

where α_s is defined as the absorbance coefficient, or the absorbance attenuation per unit length of suspension-filled fracture. If we assume the suspension is well mixed, such that the particle size distribution is well represented across the depth of the flowing suspension, then it is reasonable to expect a single value of α_s for any given ϕ and, thus, absorbance provides a direct measure of ϕ. However, if the suspended particles become segregated by size, this relationship will break down due to the inverse dependence on particle size of α_s.

2.4.3. Particle image velocimetry

Particle image velocimetry (PIV) analysis was performed using a modified version of the Matlab-based software, PIVlab (Thielicke and Stamhuis, 2014). A high-pass filter applied to the absorbance fields removed long-wavelength features and increased contrast between sand grains and the surrounding carrier fluid. The fracture image was divided into 32 × 32 pixel sub-regions. Taking the cross-correlation of each sub-region between two consecutive images yields the average displacement over the time interval between the two images. We performed PIV on the entire dataset (thousands of images) to construct a time-series of the velocity field within the fracture. For a more detailed description of particle image velocimetry analysis for concentrated suspensions see Medina et al. (2015). We note that the PIV analysis provides a depth-averaged measure of the velocity that emphasizes the velocity along the upper fracture surface and does not reveal the velocity profile across the aperture.

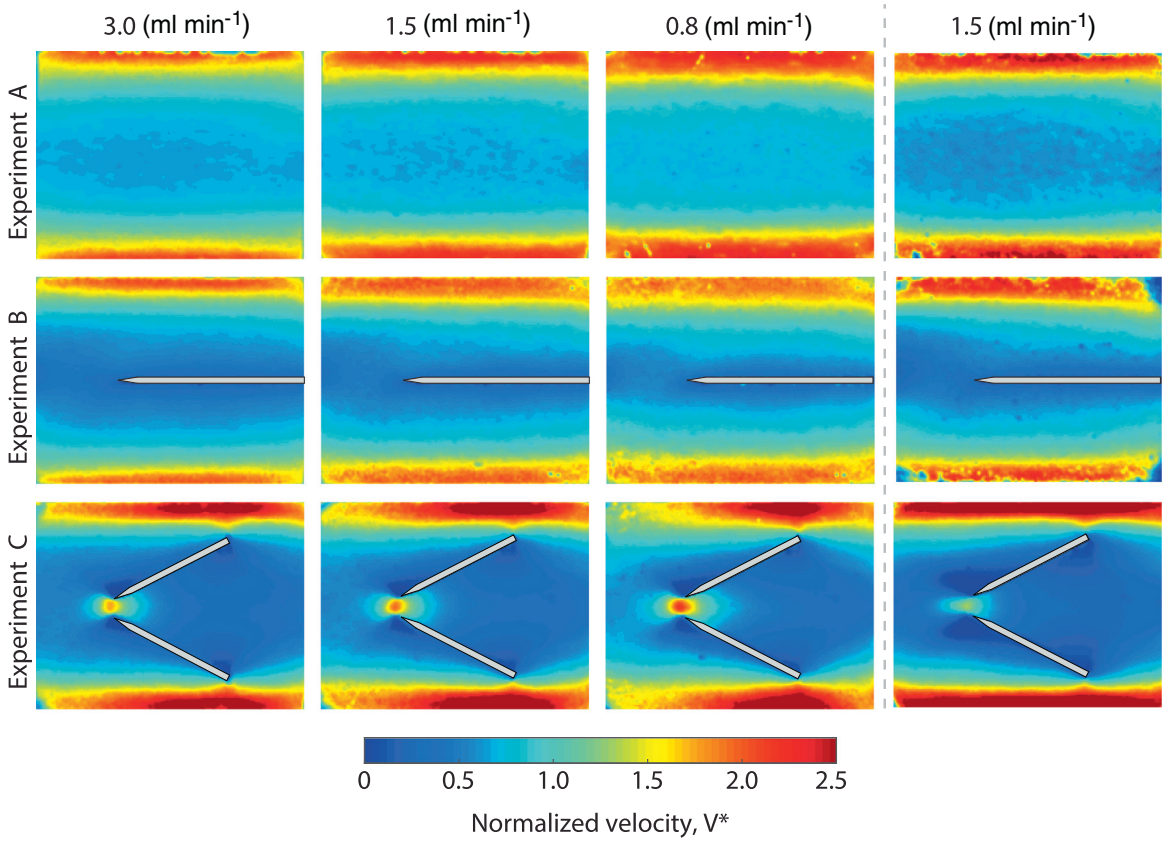

Fig. 6. Normalized velocity field for a subset of flow rates taken during the step-down and after the flow rate was increased to 1.5 ml/min, for all experiments. The velocity is normalized by the average velocity, $V^* = u/\bar{u}$, where $\bar{u} = Q/(W\langle h\rangle)$ at each flow rate. A high velocity region near the no-flow boundaries (top and bottom of each frame) is persistent at all flow rates, irrespective of obstruction placement within the fracture. (For interpretation of the references to color in this figure, the reader is referred to the web version of this article.)

3. Results

In the following sections, we summarize the results from the three experiments. We first present observations obtained from image processing, including measurements of the evolution of both the velocity fields and particle distribution throughout the duration of each experiment. We conclude with measurements of average pressure gradient over the length of the fracture for the duration of each experiment.

3.1. Velocity distribution inside the fracture

PIV analysis provided discrete measurements of the evolving velocity field within the fracture during each experiment. Averaging 30 sequential velocity fields measured at the end of each flow-rate step, provided a relatively noise-free measure of the velocity field. Fig. 6 shows normalized velocity fields, $V^* = u/\bar{u}$, where $\bar{u} = Q/(W\langle h\rangle)$, for a subset of flow rates of all three experiments. For each experiment, the time evolution of the velocity fields advances from left to right in the figure. A prominent feature in all velocity fields is the red band adjacent to the no-flow boundaries on either edge of the fracture, which indicates measured velocities greater than twice the mean velocity. These high-velocity regions occurred regardless of obstruction geometry and increased in width at lower flow rates. Despite the nonuniform velocities observed near the no-flow boundaries, the velocities measured near the fracture inlet (left-hand edge of each frame) across the middle two thirds of the fracture were relatively uniform.

For the case of the uniform, parallel-plate fracture (Exp. A), the velocity field in the middle region of the fracture (blue region) remained uniform along the entire length of the fracture, but for Exps. B and C, the velocity was affected as the suspension interacted with the obstructions. The no-slip boundaries associated with the obstructions led to narrow regions of low velocity (dark blue) surrounding each obstruction. When the obstruction was aligned parallel to the flow direction (Exp. B), this low-velocity region extended only a few millimeters from the obstruction and the remainder of the velocity field was unaffected by the presence of the obstruction resulting in a velocity field that was similar to that observed in Exp. A. For the experiment with two obstructions oriented at an angle to the flow direction (Exp. C), the obstructions caused a significant alteration of flow paths through the fracture. From the inlet, where the velocity was relatively uniform, the flow converged and accelerated through the gaps between the two obstructions and between the obstructions and the no-flow boundaries. After exiting the contraction between the two obstructions, the flow diverged to follow the expanding gap between the obstructions and gradually decelerated. The flow around the obstruction led to the formation of stagnation zones (dark blue regions) on the upstream and downstream edges of each obstruction; the stagnation zones on the upstream edges of the obstructions were significantly larger than those on the downstream edges.

As the flow rate decreased, the stagnation zones on the upstream edges of the obstructions increased in size and the localized high-velocity region between the two obstructions increased in magnitude (relative to the mean velocity). However, when the flow rate was sequentially increased after reaching a minimum flow rate of 0.2 ml/min, the velocity field exhibited hysteresis, which is evident in the difference between the two velocity fields measured at Q=1.5 ml/min. During the increasing sequence of flow rates, the

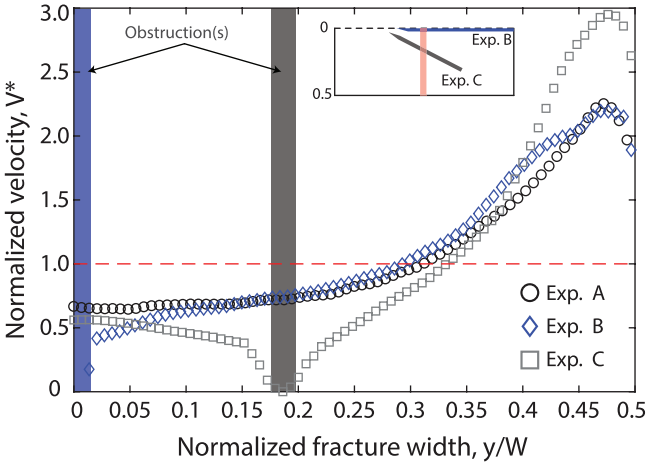

Fig. 7. Normalized velocity, V^*, profiles taken across the fracture width, sampled at $0.5L$. The sampling location is shown in Fig. 2. The different symbols show the profiles for Experiment A (black circles), Experiment B (blue diamonds), and Experiment C (gray squares). The profiles show the velocity increases symmetrically near the no-flow boundaries and span $\sim 0.15 - 0.2$ the fracture width on either side. Vertical blue and gray bands correspond to the locations of the obstructions for Exp. B and C, respectively, as shown in the inset. (For interpretation of the references to colour in this figure legend, the reader is referred to the web version of this article.)

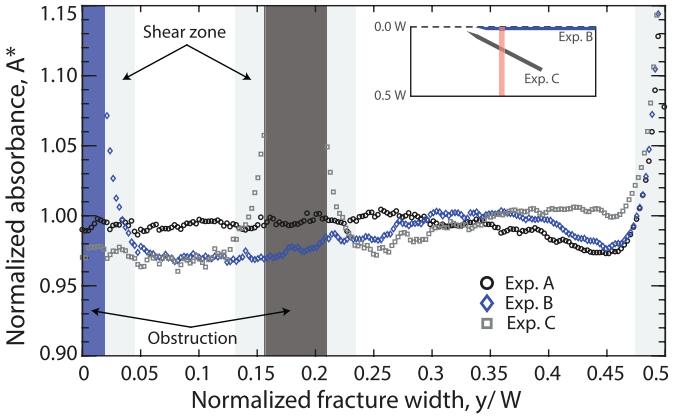

Fig. 8. Normalized absorbance, A^*, profiles sampled at $0.5L$, averaged over 1.0 cm (along the direction of flow). The absorbance was normalized by the average absorbance of each experiment. Dark blue/gray shaded areas indicate the location of the obstructions. Absorbance for Experiment A (black circles) was uniform in the middle of the fracture and decreased $\sim 3\%$ near the no-flow boundaries at $\sim 0.32W$. Absorbance for Experiment B (blue diamonds) was uniform in the middle, slowly increased and then decreased near the no-flow boundaries at $\sim 0.35W$. Absorbance in Experiment C (gray squares) was also uniform in the middle of the fracture between the obstructions; it increased slowly towards the no-flow boundaries and then decreased slightly at $0.46W$. The absorbance for all experiments in the regions immediately next to boundaries increased sharply; see text for explanation. The measurement uncertainty was $\pm 2\%$. (For interpretation of the references to colour in this figure legend, the reader is referred to the web version of this article.)

magnitude of the high-velocity region between the obstructions was significantly lower and the stagnation zones at the upstream edges of the obstructions were significantly larger. Furthermore, we note that though the two obstructions have the same angle as the inlet manifold, high-velocity regions did not form between the obstructions as observed along the boundaries at the entrance to the fracture.

To better quantify the extent of the narrow low-velocity regions surrounding the obstructions, it is useful to plot velocity profiles across the width of the fracture midway (0.5 L) along the length of the fracture (Fig. 7). Note, because the velocity profiles are symmetric about the midline of the fracture ($y = 0$), we plot the profiles from $y = 0$ to 0.5 W. The high-velocity region along the no-flow boundary extends from $\sim$ 0.35 Wto 0.5 W for each profile. The magnitude of the normalized velocity exceeds 2 for all cases and is slightly larger for Exp. C due to the acceleration of the flow through the gap between the obstruction and no-flow boundary. For Exps. B and C, the low-velocity boundary layers surrounding the obstructions are evident as the sudden drop in normalized velocity at 0 W and 0.2 W, respectively. Because the PIV analysis calculated velocity vectors in 32×32-pixel (2.4×2.4-mm) regions, we are unable to precisely resolve the extent of these boundary layers. However, Fig. 7 suggests these regions do not extend more than 4.8 mm from the obstruction. These observations are consistent with expectations for Newtonian flow within a high-aspect-ratio rectangular duct, where deviations from simple two-dimensional flow between parallel plates is limited to a region of the order of the gap width. These differences in suspension velocity in the regions adjacent to zero-slip boundaries, e.g., high velocity near the no-flow boundaries and low velocity near the obstructions, cannot explain the source source of the high-velocity region near the no-flow boundaries.

3.2. ϕ-distribution

The amount of light absorbed by the suspension is proportional to the solid volume fraction of the flowing suspension. Analyzing the absorbance across the fracture width provides a better understanding on the relationship between the ϕ-distribution and the observed velocity field. Fig. 8 shows normalized absorbance, A^*, profiles for all experiments, sampled across the fracture half-width. We normalized the absorbance by the mean absorbance of each experiment averaged over the entire fracture area, $A^* = \frac{A}{\langle A \rangle}$.

Fig. 8 revealed absorbance increased in the regions immediately next to the no-flow boundaries and obstruction walls, i.e., in the shear-zone. For a well-mixed suspension, an increase in absorbance suggests increased ϕ. However, the suspension may not be well-mixed in the regions adjacent to the boundary because shear-induced particle migration in the cross-stream direction (i.e., away from the boundary) is a function of the particle size. This size dependence leads to greater cross flow migration of large particles, similar to that observed in bi-disperse emulsions (Mohammadigoushki and Feng, 2013) and suspensions (Abbott et al., 1991; Krishnan et al., 1996). We hypothesized that preferential migration of large particles away from the high-shear region led to a retrograde migration of fine particles towards the boundary. Because absorbance is inversely proportional to the radius of the particles, $A \propto \frac{1}{a^3}$ (Eq. (4)), a small increase in the amount of fines can lead to a large increase in absorbance. To test this hypothesis, we carried out another flow through experiment (Experiment B-2) under the same experimental conditions as Experiment B but with the fines removed. Thus, the suspension had the particle size distribution shown in Fig. 4 with the fine particles ($a \lesssim 10$ μm) removed and correspondingly a lower bulk concentration of $\phi_b = 0.44$. Fig. 9 shows a region of the same absorbance profile shown in Fig. 8 for Experiment B (blue diamonds) from $y = 0$ to 0.1 Wand the corresponding absorbance profile for Experiment B-2 (red squares). The profiles show that absorbance increased $\sim 12\%$ when the fines were present and decreased $\sim 10\%$ in the absence of fine particles in a narrow region, $\mathcal{O}(h)$, next to the boundaries.

We investigated the observed deviations of the absorbance near the boundaries by measuring the absorbance of a suspension composed of fine particles *only* and a suspension with a mutlimodal PSD. We found that the absorbance for the suspension of only fine particles was approximately three times higher than the ab-

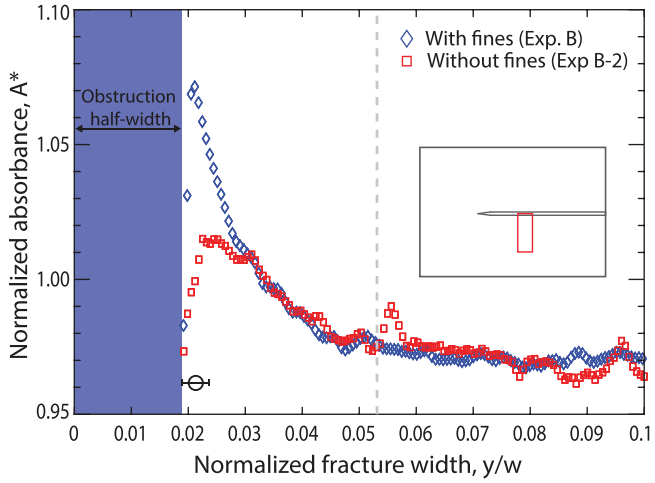

Fig. 9. Comparison of normalized absorbance profiles for two experiments with different particle size distribution. The suspension in Experiment B (same as previously presented) was composed of multimodal PSD (blue diamonds). The suspension in Experiment B-2 had a bimodal PSD (red squares). Absorbance profiles sampled immediately next to the obstruction show the absorbance of the multimodal suspension increased approximately 12%, while the absorbance of the bimodal suspension decreased approximately 10% in the region immediately next to the obstruction. The black symbol shows the size of the largest particles. The measurement uncertainty was $\pm 0.2\%$. (For interpretation of the references to colour in this figure legend, the reader is referred to the web version of this article.)

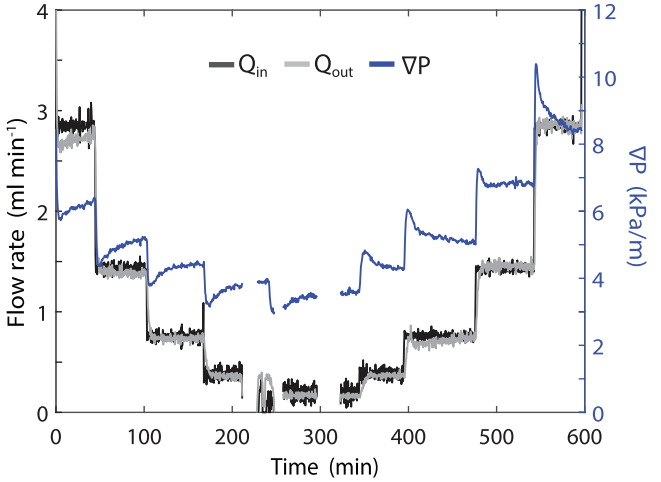

Fig. 10. Time series showing pressure gradient, ∇P (blue line), in-flow rate, Q_{in} (black line), and out-flow rate, Q_{out} (gray line), for Experiment C. Time zero is the time at which the flow rate decreased from 6.0 ml/min to 3.0 ml/min. The pressure response shows a transient behavior after every step change in flow rate which lasts up to several dozen minutes. Gaps in data were due to instrument data acquisition malfunction, however, the flow was unaffected. (For interpretation of the references to colour in this figure legend, the reader is referred to the web version of this article.)

sorbance for the suspension with multimodal PSD. These measurements and the absorbance profiles in Fig. 9, support the idea that as larger particles migrate away from the boundary (towards the 'bulk' flow), fine particles migrate in the opposite direction, towards the boundary. A mass balance calculation on a small control volume next to the obstruction, suggests that the concentration of coarse and fine particles must change by $\Delta\phi \approx 0.12$, for the absorbance to increase 12% (Figs. 8 and 9). The additional influx of large particles into the 'bulk' flow increases the concentration of coarse particles from $\phi_c = 0.440 \rightarrow 0.448$, while the concentration of fine particles decreases from $\phi_f = 0.060 \rightarrow 0.052$.

The normalized absorbance profiles across the fracture width are representative of the bulk flow, except for the light gray regions discussed above (Fig. 8). The profile for Experiment A (black circles) shows that the absorbance was uniform in the middle of the fracture ($y = 0$ to $\sim 0.32W$) and decreased by $\sim 3\%$ near the no-flow boundary. The region of uniform absorbance is consistent with the uniform velocity in the middle of the fracture and the region of decreased absorbance is consistent with the high velocity regions (Fig. 7). The normalized absorbance in Experiment B (blue diamonds) was also uniform in the middle of the fracture, it gradually increased and then decreased from $A^* = 1.015$ at $0.35W$ to $A^* = 0.975$ at $0.45W$. Experiment C (gray squares) had a uniform absorbance in the middle of the fracture, between the obstructions from $0W$ to $0.15W$. The absorbance increased on the outside of the obstructions and decreased by $\sim 1\%$ around $0.46W$, near the no-flow boundary. The observed ϕ-distribution across the fracture width is consistent with the velocity profiles for all experiments and suggests that the regions of high velocity near the no-flow boundaries are correlated with regions of decreased ϕ. Note that the diverging obstructions in Exp. C do not induce regions of low-ϕ and high-velocity near the obstructions. This suggests that the low-ϕ, high-velocity regions at the beginning of the fracture must result from a non-uniform ϕ-distribution at the inlet to the manifold.

3.3. Pressure gradient across fracture

In addition to the velocity measurements, our system allows the measurement of pressure difference between the inlet and outlet of the fracture, which yields a direct measure of the fracture-scale pressure gradient, ∇P. Fig. 10 shows the measured in-flow rate, Q_{in} (black line), out-flow rate, Q_{out} (gray line), and ∇P (blue line) over the duration of the experiment. Data for Exps. A and B showed qualitatively similar behavior, however, we present Exp. C, which had the most complete dataset (see Section 2.3 for more details).

Fig. 10 shows that after each step-change in Q_{in}, the out-flow rate (Q_{out}) reached the value of Q_{in} after a short delay ($\lesssim 5$ min). There was also a large change in ∇P over a short time, consistent with the time it took the out-flow rate to equilibrate with the in-flow rate. After the large change, ∇P slowly rebounded and approached a steady-state over a much longer timescale ($\sim 60+$ min). Fig. 11a highlights these two timescales in more detail by plotting ∇P (blue triangles) and the root mean squared deviation (RMSD) of the velocity (black circles) after decreasing the flow rate to $Q = 1.5$ ml min^{-1}. The RMSD calculates the deviation of the velocity at any given time from the velocity at the end of the flow step (e.g., steady-state). The velocity reached steady-state within minutes ($\lesssim 5$ min.) after the step change in flow rate, while ∇P changed over the duration of the flow step. Fig. 11b shows the pressure gradient normalized by the gradient at the end of the flow rate step, ∇P_{ss}, for the decreasing flow rates. The figure shows a similar transient ∇P response for all flow rate steps: initially ∇P drops to about $0.85\nabla P_{ss}$ and then slowly rebounds to reach steady state about 60 min after changing the flow rate. The measured pressure gradients suggest that the timescale to reach steady-state is insensitive to the flow rate of the suspension. Furthermore, the results also suggest that the magnitude of the early-time ∇P drop is only slightly sensitive to the flow rate.

Plotting the steady-state ∇P at the end of the flow rate reveals the pressure gradient response to the flow rate. Fig. 12 shows ∇P normalized by the specific weight of the fluid, $\rho_f g$, plotted against Reynolds number, averaged over the last four minutes at the end of each flow rate step, for Experiment B (blue triangles) and Experiment C (gray triangles). Due to data acquisition issues discussed

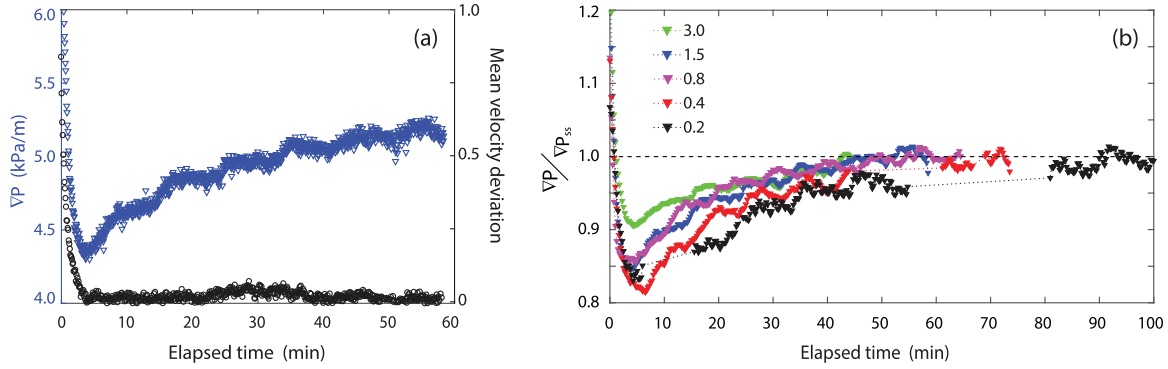

Fig. 11. (a) Pressure gradient ∇P (Blue triangles) and mean velocity deviation (root mean squared deviation) from the velocity at steady state (Black circles) after the flow rate was decreased to $Q = 1.5$ ml/min. The velocity deviation shows the velocity field reached a steady state a short time (≤ 5 min) after the flow rate was decreased. On the other hand, ∇P exhibits a short-time transient (which coincides with the velocity change) and a long-time pressure transient, which persisted over the duration of the flow rate step. (b) ∇P normalized by the steady state ∇P_{ss} (end of flow rate step) for the decreasing flow rates. The plot shows a similar trend for all flow rates. (For interpretation of the references to color in this figure legend, the reader is referred to the web version of this article.)

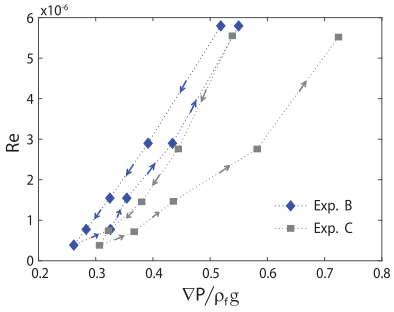

Fig. 12. Experimental pressure gradient (∇P) normalized by the specific weight of the fluid ($\rho_f g$) versus Reynolds number ($Re = \frac{\rho h \bar{u}}{\eta}$). The data shows a hysteretic behavior, which was most pronounced for Experiment C, the case with two obstructions. Both suspension exhibit a yield stress, i.e., $\frac{\nabla P}{\rho_f g} > 0$ as $Re \to 0$.

above, Experiment A was excluded in Fig. 12, but it is reasonable to expect the relationship would be similar to that of Experiment B. The arrows indicate the sequence of the experiment. Both experiments had a higher pressure gradient during the increasing portion of the stepped flow test. This hysteretic behavior was most pronounced for Experiment C, and can be explained by comparing the velocity fields for two flow rates during the decreasing and increasing stages, respectively. Column 2 in Fig. 6 shows the velocity field for $Q = 1.5$ ml/min for decreasing flow rate steps, and column 4 shows the velocity for the same flow rate during the increasing flow rate steps. As discussed in Section 3.1, these two velocity fields show clear differences. The larger jammed region in the vicinity of the stagnation zone leads to an increased pressure gradient during the increasing set of flow rates. Fig. 12 also suggests that both experiments exhibit a yield stress, i.e., non-zero ∇P as $Q \to 0$ ml/min.

Our experimental results revealed two different timescales of the transient ∇P response after a step change in flow rate: a short-time (≤ 5 mins.) transient, associated with the change in flow rate, and a long-time transient which persisted over the duration of each flow rate step. This transient ∇P behavior was observed in all experiments, irrespective of flow rate, obstruction placement, solid concentration, or particle size distribution.

4. Discussion

The experimental velocity and pressure gradient results showed unexpected behavior of the concentrated suspension. Our measurements showed the regions near the no-flow boundaries had velocities that were more than twice the average velocity. The absorbance analysis revealed these high-velocity regions were correlated to reduced ϕ in these regions. Furthermore, the angle of the manifold walls was the same as the angle of the obstructions in Exp. C, however, regions of low-ϕ (high-velocity) did not develop in the extensional region between the obstructions. Therefore, we hypothesize these low-ϕ regions were caused by the formation of non-uniform ϕ-distribution upstream of the inlet manifold. Pressure measurements across the fracture showed two characteristic timescales for ∇P in response to a step-change in flow rate. The long-time transient ∇P was observed in all experiments and was insensitive to flow rate. We hypothesize that the long-time transient ∇P behavior was caused by internal changes in the suspension, i.e., particle rearrangement as the suspension flowed through the fracture. Because we cannot quantify these changes with our experimental system, we use the two-dimensional suspension balance model (SBM) (Dbouk, 2013) in two different idealized flow geometries, to investigate the source of the high-velocity (low-ϕ) regions near the no-flow boundary and the transient ∇P observed in our experiments.

As previously discussed, shear-induced normal stress differences in suspensions cause particles to migrate from regions of high shear to regions of low shear. Guar-gum fluids also have normal stress differences, however, these differences are negligible for shear rates $\dot{\gamma} \leq 10$ sec^{-1} (Torres et al., 2014). The maximum shear rate expected in our experiments was ~ 1.0 sec^{-1}; therefore, we assume normal stress differences arising from the fluid are negligible and are ignored. We modified the SBM model to include the shear-dependent fluid viscosity for 0.75% guar-gum solution, which is approximated by the Cross-power law model (Fig. 3). This SBM model assumes uniform-sized particles; we used the weighted geometric mean of the particle radii ($a = 56\,\mu$m) as an approximation of the multimodal PSD used in the experiments.

We used the suspension balance model to simulate a 2-D version of the geometry described in Section 2.1. The geometries of Experiments A, B, and C correspond to Models A, B, and C, respectively. For all three models, flow was along the x-axis and the fracture width was aligned with the y-axis, such that shear acted in the $x - y$ plane (e.g., fracture plane). We plot the concentration profiles for all three simulations, normalized by the inlet concentration $\phi_0 = 0.5$ (Fig. 13). The profiles show a slight concentration decrease at the obstruction boundaries in Model B and Model C, which are consistent with that observed for Exp. B-2 (Fig. 9). Though there are slight differences, ϕ^* profiles for all three simulations show the regions adjacent to the no-flow boundaries have a significantly lower ϕ^* than the middle regions. The normal-

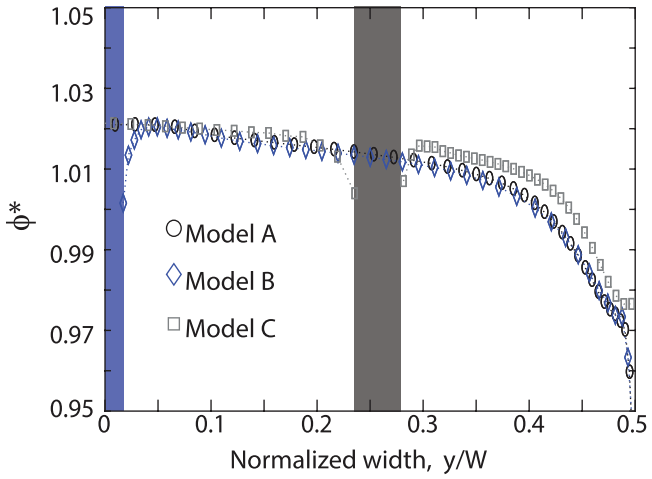

Fig. 13. Normalized concentration, $\phi^* = \frac{\phi}{\phi_0}$, profiles sampled across the fracture width at $0.5L$ for all three models. The profiles show ϕ^* decreased $\sim$4% at $0.35W$ (Model A), at $0.35W$ (Model B), and $0.40W$ (Model C), respectively.

ized concentration profiles show ϕ^* decreased by approximately 4% near the no-flow boundary for all simulations (Fig. 13). These low-ϕ regions spanned approximately $0.1W$-$0.12W$ on either side, similar to that observed in the experiments (Fig. 8).

As with the experiments, the obstructions did not develop low-ϕ regions similar to those next to the no-flow boundaries. This difference is best illustrated by Model C: the obstructions have the same expansion ratio (i.e., same angle) as the inlet manifold and both are no-slip boundaries. Flow through the manifold and in the region between the obstructions has similar extensional flow components. The reason low-ϕ regions developed adjacent to the no flow boundaries and *not* between the obstructions is due to upstream solid distribution. The simulation included a long tube, upstream of the manifold. As the suspension flowed inside the tube it developed a non-uniform ϕ-distribution which was then extended inside the manifold. Therefore, when the suspension reached the fracture entrance at $L = 0$, the concentration was already non-uniform across the width. In contrast, upstream of the obstructions the suspension was uniform, this was confirmed by both the simulation and experimental results (Section 3.2). Thus, the low-ϕ regions observed in both the simulations and experiments were not caused by the manifold, they developed inside the tube and were extended laterally as they flowed through the manifold.

We investigate the cause of the long-time transient pressure gradients observed in our experiments by simulating a long, rectangular, 2-D channel oriented in the $x - z$ plane (e.g., aperture plane) with the same height as the fracture aperture, $h = 0.34$ cm. We imposed a parabolic velocity profile, $u_x(z)$, and a uniform solid volume fraction $\phi_0 = 0.5$ at the inlet. We simulated injecting the suspension at a flow rate of $Q = 6.0$ ml/min until it reached steady-state. The step-decrease in flow rate was simulated as an instantaneous decrease in velocity, corresponding to a flow rate of $Q = 3.0$ ml/min. We investigate the effect of gravity by simulating the suspension with particles that are denser than the fluid and the suspension with neutrally buoyant particles. For more details on the simulations see supplementary material.

Fig. 14 shows the evolution of the suspension concentration and the effect this evolution has on the pressure after a step change in flow rate from 6 to 3 ml/min. Fig. 14a shows the evolution of the ϕ−profile across the fracture aperture. We sampled the concentration one meter into the fracture, which results in a travel time from the inlet to the observation point that is similar to the timescale required for suspension in the experiment to travel from the pump to the observation point in the fracture. For the neutrally buoyant suspension there was almost no change from the previously established steady-state ϕ-distribution (Fig. 14a2), whereas, for the dense suspension, the ϕ-distribution evolved over time (Fig. 14a1). Because the decreased velocity leads to reduced shear rate, shear-induced particle stresses decrease and gravity causes particles to migrate towards the lower fracture surface. This particle migration leads to the formation of a region with higher solid concentration on the bottom surface (Fig. 14b1).

Changes in the ϕ-distribution led to corresponding changes in the velocity distribution (Fig. 14b3), therefore, it is instructive to consider the evolution of the shear stress, $\tau = \dot{\gamma}\eta(\phi, \dot{\gamma})$, across the aperture. Fig. 14c shows the shear stress normalized by a characteristic shear stress, $\tau_0 = \dot{\gamma}_0\eta(\phi_0, \dot{\gamma}_0)$, where shear rate is approximated by $\dot{\gamma}_0 = \frac{3\bar{u}}{h}$ and $\phi_0 = 0.5$ is the inlet concentration. The shear stress distribution for the suspension with neutrally buoyant particles remained constant throughout the duration of the flow step (Fig. 14c2). Whereas, the shear stress distribution for the dense suspension shows the development of a high shear stress region at the bottom of the fracture (Fig. 14c1). This high shear stress region at the bottom fracture surface suggests gravity-driven particle migration leads to an extended region with an increased solid content (blue circles in Fig. 14b1).

Fig. 14d shows the pressure gradient sampled at $x = 1.0$ m. The plot shows a large step-decrease in ∇P, caused by the instantaneous decrease in velocity (flow rate decreased from $Q = 6.0 \rightarrow 3.0$ ml/min at time $t = 0$). For the neutrally-buoyant suspension ∇P remained almost constant after the initial decrease, but for the suspension with dense particles ∇P gradually rebounds to an intermediate value. The magnitude of the rebound is consistent with that observed in the experiments. Furthermore, the time evolution of the ϕ-distribution and its effect on the shear stress support the conclusion that the transient ∇P observed during the experiments was due to a gradual redistribution of ϕ, which caused a corresponding increase in shear stress on the bottom surface of the fracture.

The pressure gradient plot for the stepped flow experiment shows that ∇P reached a steady state over a timescale that is independent of flow rate (Fig. 11b). This suggests that the timescale of particle rearrangement across the fracture after each flow rate change is also time independent. The two mechanisms controlling cross-flow transport of suspended particles are: shear-induced normal stress differences, which drive particle motion from regions of high shear-rate to regions of low shear-rate and gravity driven particle settling. Shear-induced particle migration can be approximated as a diffusive process, in which particles must travel a distance of half the aperture, $h/2$, before the suspension reaches its fully developed distribution (Nott and Brady, 1994). For a concentrated suspension this timescale is given by $t_{diff} \sim \frac{h^3}{a^2}\frac{1}{4\bar{u}}$ (Leighton and Acrivos, 1986). The corresponding timescale for gravity driven migration is given by $t_{set} = \frac{h}{u_s f(\phi)}$, where $u_s = 2g\Delta\rho a^2/9\eta_f$ is the Stokes settling velocity of a single particle, $f(\phi)$ is the hindrance function (see Eq. (5) in supplementary material), and their product is the hindered settling velocity. Note, η_f depends on $\dot{\gamma}$, but for the settling of particles flowing with the suspension, $\dot{\gamma}$ scales with the settling velocity, not the flow rate such that η_f can be approximated by η_{f_o}.

We can quantify the relative effect of shear-induced particle migration to gravity-driven settling by taking the ratio of the diffusive and settling timescales:

$$t^* = \frac{t_{diff}}{t_{set}} = \frac{2h^2 g\Delta\rho}{9\eta_f \bar{u}}\frac{f(\phi)}{4} \tag{5}$$

Since both timescales depend on the square of the particle size, taking the ratio of the diffusive and settling timescales removes the particle size dependence. Furthermore, when $t^* = O(1)$ both the

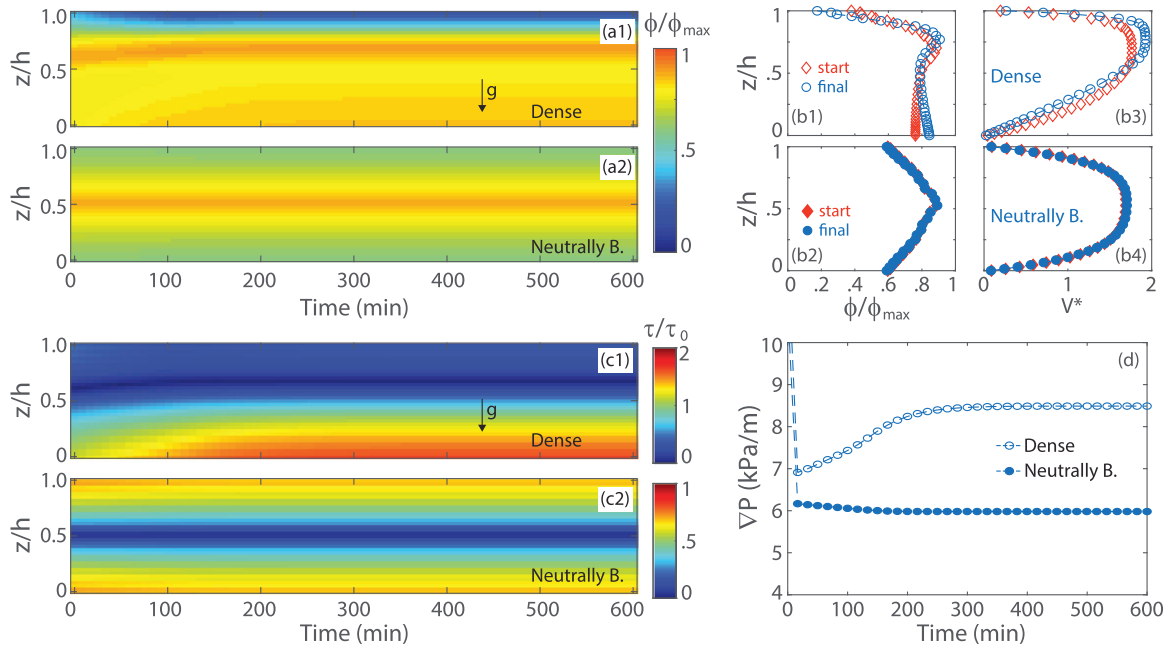

Fig. 14. Simulation results for a concentrated ($\phi_0 = 0.5$) suspension flowing inside a long rectangular channel, after a step change in flow rate $Q = 6.0 \rightarrow 3.0$ ml/min. (a1-2) Normalized concentration distribution, ϕ/ϕ_{max}, across the fracture aperture; sampled at $x = 1.0$ m; (b1-2) normalized concentration profiles, ϕ/ϕ_{max} and (b3-4) normalized velocity profiles, $V^* = u/\bar{u}$; (c1-2) normalized shear stress, τ/τ_0; and (d) pressure gradient, ∇P. (For interpretation of the references to colour in this figure, the reader is referred to the web version of this article.)

settling and diffusive timescales are of the same order of magnitude. In the experiments, the diffusive timescale is smaller than the settling timescale ($t^* = 0.04$) at the highest flow rate, while at the lowest flow rate, both timescales were of the same order of magnitude ($t^* = 1.21$). This suggests the settling timescale controls the transient behavior observed in our experiments. This is supported by Fig. 11b, which shows the transient timescale is independent of the average velocity. In the experiments, the time it takes the transient ∇P to reach steady-state is on the order of 60 min. This is the time it takes the larger particles in the concentrated suspension to settle a distance equal to the fracture aperture, h. This suggests that even in a multimodal dense suspension, settling of the larger particles controls the timescale required to reach steady state.

Changing the alignment of the shear plane in a two-dimensional suspension balance model provided additional insights to the complexities of three-dimensional suspension flows. Aligning the shear plane with the fracture plane, the simulations demonstrated the development of the non-uniform ϕ-distribution across the fracture width, similar to that observed in our experiments. The simulations show that the low-ϕ regions on either side of the fracture, spanning 15% of the width, developed in the upstream tubing and expanded laterally as the suspension flowed through the diverging manifold. Aligning the shear plane with the aperture plane, demonstrated that particle rearrangement due to setting controls the evolution of ϕ across the fracture aperture. This evolving ϕ-distribution changed the shear-stress distribution and directly impacted the long-time transient ∇P response observed in our experiments.

5. Conclusion

We studied the flow behavior of a concentrated suspension flowing inside a laboratory-scale analog fracture. The use of a transparent fracture allowed the direct quantification of ϕ field, velocity field, and the evolving pressure gradient as the suspension flowed through different flow geometries. Obstructions placed in the fracture flow field added shear-rate gradients in both cross-flow directions and extensional components to the flow. The experiments demonstrated that both the orientation of the obstructions and the development of non-uniform ϕ-distributions within the fracture had significant effects on the velocity and ∇P of the flowing suspensions.

Applying transmitted-light techniques allowed direct quantification of the solid concentration. Absorbance measurements captured particle-size-dependent shear-induced migration in the regions adjacent to no-flow boundaries, in which larger particles preferentially migrated from regions of high shear to regions of lower shear (e.g., away from the walls). This size-dependent migration is similar to that observed in concentric cylinders (Abbott et al., 1991) and parallel plates (Krishnan et al., 1996). Furthermore, our analysis suggests that in dispersed suspensions, larger particles migrating away from the walls displace smaller particles towards the walls, opposite to the expected shear-induced motion. This led to a small region adjacent to the walls with a higher concentration of small particles and depleted of larger particles.

Velocity measurements revealed that the regions near the no-flow boundaries (spanning approximately 15% of the fracture width on either side) had the highest velocity, whereas the middle two-thirds of the fracture had a uniform velocity. Absorbance measurements revealed these high velocity regions were correlated with lower ϕ in these regions. Though a lower ϕ was expected near the no-flow boundaries, the extent of these low-ϕ regions was unexpected. Using the two dimensional SBM in the fracture plane, demonstrated that the non-uniform ϕ distribution formed in the inlet tubing, and was subsequently extended laterally as the suspension transition into the gradually expanding manifold. This led to relatively wide regions of lower ϕ near the walls and uniform ϕ in the middle of the fracture. This suggest that non-uniform ϕ-distributions may have a large impact on the velocity and lateral solid concentration distribution that may persist over long timescales and lengthscales. This is especially important in hy-

draulic fracturing where the solid distribution can have a significant effect on the permeability of the propped fracture.

The pressure gradient, ∇P, across the fracture exhibited a transient response after a step-change in flow rate. This transient behavior persisted throughout the experiment and was insensitive to flow rate or obstruction configuration. Simulating a long 2-D channel showed that the spatial-temporal evolution of ϕ-distribution across the fracture aperture was directly related to the transient ∇P response after a step-change in flow rate. As the flow rate decreased, the shear-induced particle forces decreased, compared to the gravitational forces, which led to a downward flux of particles and the formation of a region with higher concentration near the bottom fracture surface. A scaling analysis showed that for the range of experimental flow rates, the settling timescale was comparable to or larger than the 'diffusive' timescale. Therefore, the time required for ∇P to reach steady-state was controlled by the settling timescale of the larger particles in the suspension.

Though existing formulations of the suspension balance model do not allow for fully 3-D flows, our results demonstrate that important features of our experiments can be represented using 2-D idealizations of the flow geometry. We note that this approach does not represent effects arising from concurrent shear-rate gradients in the fracture plane and across the fracture aperture. These may be important, particularly in regions where large changes in ϕ in the fracture plane lead to significant in-plane velocity variations or in the vicinity of no-flow boundaries (e.g., areas of contact between fracture surfaces). Nonetheless, 2-D simulations can provide significant insights into the mechanisms controlling the distribution of suspended solids within fractures and the potential impact on velocity fields and pressure gradients. Understanding this connection between ϕ distribution and the relationship between pressure gradients and suspension velocities is important in both engineering applications (e.g., hydraulic fracturing) and natural events (e.g., mud volcanoes) where at least one of these measurements is unknown.

Acknowledgments

The authors gratefully acknowledge the financial support of Schlumberger-Doll Research grant no. SCH-53986 and the Department of Civil and Environmental Engineering at University of California, Irvine.

Supplementary material

Supplementary material associated with this article can be found, in the online version, at 10.1016/j.ijmultiphaseflow.2018.06.014.

References

Abbott, J.R., Tetlow, N., Graham, A.L., Altobelli, S.A., Fukushima, E., Mondy, L.A., Stephens, T.S., 1991. Experimental observations of particle migration in concentrated suspensions: Couette flow. J. Rheol. (N Y N Y) 35 (5), 773–795. doi:10.1122/1.550157.

Bayliss, L., 1965. The flow of suspensions of red blood cells in capillary tubes. changes in the 'cell-free' marginal sheath with changes in the shearing stress.. J. Physiol. (Lond.) 179 (1), 1.

Bohren, C.F., Huffman, D.R., 2008. Absorption and Scattering of Light by Small Particles. John Wiley & Sons.

Boyer, F., Guazzelli, E., Pouliquen, O., 2011. Unifying suspension and granular rheology. Phys. Rev. Lett. 107, 188301. doi:10.1103/PhysRevLett.107.188301.

Brady, J.F., Morris, J.F., 1997. Microstructure of strongly sheared suspensions and its impact on rheology and diffusion. J. Fluid Mech. 348, 103–139. doi:10.1017/S0022112097006320.

Chang, C., Powell, R.L., 1993. Dynamic simulation of bimodal suspensions of hydrodynamically interacting spherical particles. J. Fluid Mech. 253, 1–25. doi:10.1017/S0022112093001697.

Chapman, B.K., Leighton, D.T., 1991. Dynamic viscous re-suspension. Int. J. Multiph. Flow 17 (4), 469–483. doi:10.1016/0301-9322(91)90043-3.

Chhabra, R.P., 2006. Bubbles, drops, and particles in Non-Newtonian fluids. Chemical Industries. CRC Press. Second ed.

Chong, J.S., Christiansen, E.B., Baer, A.D., 1971. Rheology of concentrated suspensions. J. Appl. Polym. Sci. 15 (8), 2007–2021. doi:10.1002/app.1971.070150818.

Chow, A., Iwayima, J., Sinton, S., Leighton, D., 1995. Particle migration of non-Brownian, concentrated suspensions in a truncated cone-and-plate. In: Proceedings of the Society of Rheology Meeting, Sacramento, CA, 103.

Dagois-Bohy, S., Hormozi, S., Guazzelli, É., Pouliquen, O., 2015. Rheology of dense suspensions of non-colloidal spheres in yield-stress fluids. J. Fluid Mech. 776. doi:10.1017/jfm.2015.329.

Dbouk, T., 2013. Rheology of Concentrated Suspensions and Shear-Induced Migration. Ph.D. thesis. Citeseer.

Detwiler, R.L., Pringle, S.E., Glass, R.J., 1999. Measurement of fracture aperture fields using transmitted light: an evaluation of measurement errors and their influence on simulations of flow and transport through a single fracture. Water Resour. Res. 35 (9), 2605–2617. doi:10.1029/1999WR900164.

Einstein, A., 1906. Eine neue bestimmung der moleküldimensionen. Ann. Phys. 324 (2), 289–306.

Frankel, N.A., Acrivos, A., 1970. The constitutive equation for a dilute emulsion. J. Fluid Mech. 44, 65–78. doi:10.1017/S0022112070001696.

Gadala-Maria, F., Acrivos, A., 1980. Shear-induced structure in a concentrated suspension of solid spheres. J. Rheol. (N Y) 24 (6), 799–814. doi:10.1122/1.549584.

Gamonpilas, C., Morris, J.F., Denn, M.M., 2016. Shear and normal stress measurements in non-Brownian monodisperse and bidisperse suspensions. J. Rheol. (N Y N Y) 60 (2), 289–296. doi:10.1122/1.4942230.

Garland, S., Gauthier, G., Martin, J., Morris, J.F., 2013. Normal stress measurements in sheared non-Brownian suspensions. J. Rheol. (N Y) 57 (1), 71–88. doi:10.1122/1.4758001.

Graham, D., Jones, T., 1994. Settling and transport of spherical particles in power-law fluids at finite Reynolds number. J. Non-Newton Fluid Mech. 54 (0), 465–488. doi:10.1016/0377-0257(94)80037-5.

Hampton, R.E., Mammoli, A.A., Graham, A.L., Tetlow, N., Altobelli, S.A., 1997. Migration of particles undergoing pressure-driven flow in a circular conduit. J. Rheol. (N Y) 41 (3), 621–640. doi:10.1122/1.550863.

Kaushal, D., Sato, K., Toyota, T., Funatsu, K., Tomita, Y., 2005. Effect of particle size distribution on pressure drop and concentration profile in pipeline flow of highly concentrated slurry. Int. J. Multiph. Flow 31 (7), 809–823. doi:10.1016/j.ijmultiphaseflow.2005.03.003.

Koh, C.J., Hookham, P., Leal, L., 1994. An experimental investigation of concentrated suspension flows in a rectangular channel. J. Fluid Mech. 266 (1), 1–32. doi:10.1017/S0022112094000911.

Krieger, I.M., Dougherty, T.J., 1959. A mechanism for non-Newtonian flow in suspensions of rigid spheres. Trans. Soc. Rheol. (1957–1977) 3 (1), 137–152. doi:10.1122/1.548848.

Krishnan, G.P., Beimfohr, S., Leighton, D.T., 1996. Shear-induced radial segregation in bidisperse suspensions. J. Fluid Mech. 321, 371–393. doi:10.1017/S0022112096007768.

Lecampion, B., Garagash, D.I., 2014. Confined flow of suspensions modelled by a frictional rheology. J. Fluid Mech. 759, 197–235. doi:10.1017/jfm.2014.557.

Leighton, D., Acrivos, A., 1986. Viscous re-suspension. Chem. Eng. Sci. 41 (6), 1377–1384. doi:10.1016/0009-2509(86)85225-3.

Leighton, D., Acrivos, A., 1987. Measurement of shear-induced self-diffusion in concentrated suspensions of spheres. J. Fluid Mech. 177, 109–131. doi:10.1017/S0022112087000880.

Lyon, M.K., Leal, L.G., 1998. An experimental study of the motion of concentrated suspensions in two-dimensional channel flow. part 1. monodisperse systems. J. Fluid Mech. 363, 25–56. doi:10.1017/S0022112098008817.

Mader, H., Llewellin, E., Mueller, S., 2013. The rheology of two-phase magmas: a review and analysis. J. Volcanol. Geotherm. Res. 257 (0), 135–158. doi:10.1016/j.jvolgeores.2013.02.014.

Medina, R., Elkhoury, J.E., Morris, J.P., Prioul, R., Desroches, J., Detwiler, R.L., 2015. Flow of concentrated suspensions through fractures: small variations in solid concentration cause significant in-plane velocity variations. Geofluids 15 (1,2), 24–36. doi:10.1111/gfl.12109.

Medina, R., Elkhoury, J.E., Morris, J.P., Prioul, R., Desroches, J., Detwiler, R.L., 2016. Flow of concentrated suspensions through fractures: small variations in solid concentration cause significant in-plane velocity variations. In: Gleeson, T., Ingebritsen, S. (Eds.), Crustal Permeability. John Wiley & Sons, pp. 27–38.

Metzner, A.B., 1985. Rheology of suspensions in polymeric liquids. J. Rheol. (N Y) 29 (6), 739–775. doi:10.1122/1.549808.

Miller, R.M., Morris, J.F., 2006. Normal stress-driven migration and axial development in pressure-driven flow of concentrated suspensions. J. Non-Newton Fluid Mech. 135 (2–3), 149–165. doi:10.1016/j.jnnfm.2005.11.009.

Mohammadigoushki, H., Feng, J.J., 2013. Size segregation in sheared two-dimensional polydisperse foam. Langmuir 29 (5), 1370–1378. doi:10.1021/la304445f.

Morris, J.F., Boulay, F., 1999. Curvilinear flows of noncolloidal suspensions: the role of normal stresses. J. Rheol. (N Y) 43 (5), 1213–1237. doi:10.1122/1.551021.

Murdoch, L., 1995. Alternative Methods for Fluid Delivery and Recovery. DIANE Publishing.

Nott, P.R., Brady, J.F., 1994. Pressure-driven flow of suspensions: simulation and theory. J. Fluid Mech. 275, 157–199. doi:10.1017/S0022112094002326.

Oh, S., Song, Y.-q., Garagash, D.I., Lecampion, B., Desroches, J., 2015. Pressure-driven suspension flow near jamming. Phys. Rev. Lett. 114, 088301. doi:10.1103/PhysRevLett.114.088301.

Pal, R., 2015. Rheology of suspensions of solid particles in power-law fluids. Can. J. Chem. Eng. 93 (1), 166–173. doi:10.1002/cjce.22114.
Pearson, J., 1994. On suspension transport in a fracture: framework for a global model. J. Non-Newton Fluid Mech. 54 (0), 503–513. doi:10.1016/0377-0257(94)80039-1.
Perez, R., Siquier, S., Ramirez, N., Muller, A., Saez", A., 2004. Non-Newtonian annular vertical flow of sand suspensions in aqueous solutions of guar gum. J. Petrol. Sci. Eng. 44 (3–4), 317–331. doi:10.1016/j.petrol.2004.03.006.
Phillips, R.J., Armstrong, R.C., Brown, R.A., Graham, A.L., Abbott, J.R., 1992. A constitutive equation for concentrated suspensions that accounts for shear-induced particle migration. Phys. Fluids A 4 (1), 30–40. doi:10.1063/1.858498.
Quemada, D., 1977. Rheology of concentrated disperse systems and minimum energy dissipation principle. Rheol. Acta 16 (1), 82–94. doi:10.1007/BF01516932.
Reddy, M.M., Singh, A., 2014. Flow of concentrated suspension through oblique bifurcating channels. AlChE J. 60 (7), 2692–2704. doi:10.1002/aic.14446.
Siginer, D.A., 2015. Developments in the Flow of Complex Fluids in Tubes. Springer.
Thielicke, W., Stamhuis, E.J., 2014. PIVlab - Towards User-friendly, Affordable and Accurate Digital Particle Image Velocimetry in MATLAB. Journal of Open Research Software 2 (1), e30. doi:10.5334/jors.bl.
Torres, M., Hallmark, B., Wilson, D., 2014. Effect of concentration on shear and extensional rheology of guar gum solutions. Food Hydrocoll. 40, 85–95. doi:10.1016/j.foodhyd.2014.02.011.
Wong, R.C.K., Alfaro, M.C., 2001. Fracturing in low-permeability soils for remediation of contaminated ground. Can. Geotech. J. 38 (2), 316–327. doi:10.1139/t00-097.
Yadav, S., Reddy, M.M., Singh, A., 2015. Shear-induced particle migration in three-dimensional bifurcation channel. Int. J. Multiph. Flow 76, 1–12. doi:10.1016/j.ijmultiphaseflow.2015.06.007.
Zarraga, I.E., Hill, D.A., Jr., D.T.L., 2000. The characterization of the total stress of concentrated suspensions of noncolloidal spheres in Newtonian fluids. J. Rheol. (N Y) 44 (2), 185–220. doi:10.1122/1.551083.